Composites: Part B 43 (2012) 3467–3481

Contents lists available at SciVerse ScienceDirect

Composites: Part B

journal homepage: www.elsevier.com/locate/compositesb

Quasi-static and dynamic fracture behavior of particulate polymer composites: A study of nano- vs. micro-size filler and loading-rate effects

Kailash C. Jajam, Hareesh V. Tippur *

Department of Mechanical Engineering, Auburn University, Auburn, AL 36849, USA

ARTICLE INFO

Article history:
Received 17 October 2011
Received in revised form 21 December 2011
Accepted 2 January 2012
Available online 10 January 2012

Keywords:
A. Polymer–matrix composites (PMCs)
A. Particle-reinforcement
B. Fracture
B. Impact behaviour
Micro- vs. nano-composites

ABSTRACT

The role of nano- vs. micro-filler particle size-scale on static and dynamic fracture behaviors of silica-filled epoxy is examined. Particulate composites of epoxy matrix are studied under quasi-static and stress-wave loading conditions. Mode-I crack initiation and crack growth behaviors are examined using 2D digital image correlation method and high-speed photography in symmetrically impacted specimens. The measured displacement fields are analyzed using 2D crack-tip fields for dynamically propagating cracks in brittle solids to extract stress intensity factor (K_I^d) histories, and crack velocity histories (V). K_I^d–V plots for each type of composite are also presented. The quasi-static fracture tests show fracture toughness enhancement in case of nanocomposites relative to micro-particle filled ones. On the other hand, the dynamic crack-initiation toughness is consistently higher for micro-particle filled composites relative to the nano-filler counterparts. These counterintuitive results are supported by crack velocity histories in nanocomposites being significantly higher than that observed in micro-filler cases. The characteristic K_I^d–V profiles suggest higher terminal velocities and lower dynamic fracture toughness for nanocomposites. Also, the post-mortem analyses of fracture surfaces reveal greater surface ruggedness for nanocomposites under quasi-static conditions. However, the opposite is evident under dynamic loading conditions. The qualitative and quantitative fractographic measurements correlate well with the measured fracture parameters for both quasi-static and dynamic fracture tests.

1. Introduction

Particulate polymer composites (PPCs) generally consist of micro- or nano-fillers of different sizes and shapes randomly dispersed in polymer matrices. Over the years there has been considerable interest in these materials since the dispersed fillers can be used to easily control the overall stiffness, strength, fracture toughness and impact energy absorption of the resulting composite. Most reports to date deal with PPCs made of micron-size particles. Recent advances in materials processing techniques, however, have made it possible to reduce particle dimensions to nano-scale providing high specific surface area. It has also been well established that rigid inorganic fillers provide macroscopic isotropy as well as enhanced fracture toughness and high energy absorption capabilities to brittle polymers [1–4]. Past studies [5–9] on micron-size particle filled composites suggest that fracture toughness is essentially governed by filler particle shape, size, volume fraction and filler–matrix interfacial strength. However, particle size in the nano-scale could vary the mechanical response in general and fracture behavior in particular depending upon the nature of loading, quasi-static or dynamic. In view of this, the current work is aimed towards examining the role of filler size-scale (nano- vs. micro-) on fracture response of PPCs under quasi-static and dynamic loading conditions.

Investigations pertaining to mechanical and fracture behaviors of nanocomposites and associated toughening mechanisms reported in the literature are briefly reviewed in the following. Recently, Hsieh et al. [10] have studied the toughening mechanisms of epoxies modified with silica nanoparticles of mean diameter 20 nm. They have reported steady increase in elastic modulus, quasi-static fracture toughness, K_{Ic}, and fracture energy, G_{Ic} with particle volume fraction (V_f) and identified localized shear bands and debonding of particles leading to void growth as the main toughening mechanisms. Reynaud et al. [11] used in situ polymerization technique to produce nanocomposites consisting of nano-silica (12–50 nm) embedded in polyamide 6. They observed enhanced tensile yield strength with decreasing particle size and suggest that multiple debonding occurs throughout the clusters of 12 nm particles, whereas 50 nm filler particles do not aggregate and each particle undergoes a single debonding process. Boesl et al. [12] and Liu et al. [13] noted enhanced fracture response of nano-size ZnO (53 nm) and nano-silica (20 nm) modified epoxies, respectively. Rosso et al. [14] examined the effect of 5% V_f silica nanoparticles (~50 nm) on quasi-static fracture of Araldite-F epoxy and noted

* Corresponding author. Tel.: +1 334 844 3327; fax: +1 334 844 3307.
E-mail addresses: jajamkc@auburn.edu (K.C. Jajam), tippuhv@auburn.edu (H.V. Tippur).

1359-8368/$ - see front matter © 2012 Elsevier Ltd. All rights reserved.
doi:10.1016/j.compositesb.2012.01.042

70% and 140% improvement in K_{Ic} and G_{Ic}, respectively. The incorporation Al_2O_3 (13 nm) and TiO_2 (200–500 nm) nanoparticles in epoxy by Wetzel et al. [15] showed improved flexural stiffness and strength as well as quasi-static fracture toughness and fracture energy. Their work pointed out crack-tip blunting, crack deflection and crack pinning as major sources of toughening. Liang and Pearson [16] incorporated two particle sizes of nanosilica (20 and 80 nm) to study the size effect on toughening mechanisms of epoxy–silica nanocomposites. They demonstrated that both particle sizes improved K_{Ic} and G_{Ic} with volume fraction due to matrix plastic deformation led zone shielding toughening mechanism but particle size showed negligible effect on variation of fracture toughness. Tsai et al. [17] noted enhanced mechanical properties and fracture toughness for nanosilica (25 nm) reinforced epoxies. The fracture response of bidispersed nano- and micro-filler epoxies examined by Kwon et. al. [18] found to be dependent on the particle–matrix interactions as well as on temperature. Johnsen et al. [19] carried out mechanical and fracture studies on nanosilica (20 nm) filled-epoxies up to 13% V_f and observed enhanced K_{Ic} and G_{Ic} due to void growth and particle–matrix debonding. A review by Jordan et al. [20] on experimental trends in polymer nanocomposites highlights issues associated with processing and mechanical responses of nano- vs. micron-sized particulate composites. They summarized that nanocomposites serve better in some mechanical aspects than the micron-sized counterparts. However, no universal trends were established as nanocomposites showed large deviations in properties due to physical and chemical differences between the constituent phases and fabrication challenges. Similarly, more recent reviews by Sun et al. [21] and Fu et al. [22] suggest that energy absorption characteristics of nanocomposites under quasi-static or impact loading conditions depends on key parameters such as shape, dimension of nanoparticles, mechanical properties of the filler and the host matrix, filler-matrix interfacial strength, as well as volume fraction and particle dispersion in the matrix.

A few comparative studies have also been carried out to understand the effects of size-scale and particle volume fraction on the fracture behavior and fracture toughness of nano- and micro-particle-filled composites under quasi-static loading conditions. For example, Singh et al. [23] reinforced polyester resin with aluminum particles of nano- (100 nm) and micron-sizes (3.5 and 20 μm). They noted monotonic increase in K_{Ic} with volume fraction for a given particle size and higher K_{Ic} in the case of nano-filled composites than the micron-sized ones up to a volume fraction of 2.3%. Adachi et al. [24] studied quasi-static fracture behavior of nano- and micro-spherical silica-filled epoxies and observed improved K_{Ic} in the nano-filler cases than the micron-size counterparts. In contrast, Hussain et al. [25] investigated fracture behavior of particle-filled epoxy composites by varying TiO_2 filler volume fraction and particle size (20 nm and 1 μm). They found that composites with micron size particles exhibited higher fracture toughness with increasing volume fraction than the nanoparticle counterparts. Mechanical response of nano- and micron-size TiO_2 (32 nm and 0.24 μm) particle loaded epoxies was compared by Ng et al. [26,27]. They indicate that nano-particle filled epoxy show higher stiffness, failure strain and toughness when compared the one with to micron-sized ones.

Among the few dynamic fracture investigations reported on particulate composites include the study of filler particle size on the mode-I fracture behavior of glass-filled epoxy studied by Kitey and Tippur [28]. They have shown that micron-size spherical glass beads of different mean diameter in the range of 11–200 μm improved the fracture toughness of epoxy and noted that fracture toughness was the highest at an optimum particle size (35 μm) at a fixed volume fraction (10%). In regards to nanocomposites, dynamic fracture work has been reported by Shukla et al. [29] using TiO_2 (35 nm) and Al_2O_3 (14 nm) nanoparticles. Their results indicate improved fracture toughness and higher crack velocity in nano-filler cases when compared to the neat resin. Evora and Shukla [30] performed quasi-static and dynamic fracture studies on TiO_2 (36 nm) nanoparticle filled-polyester nanocomposites and observed higher fracture toughness under dynamic loading compared to the quasi-static cases. In a similar dynamic fracture work using TiO_2 (36 nm) nanoparticles in polyester resin, Evora et al. [31] reported a relationship between mode-I dynamic stress intensity factor and crack velocity and noted higher crack velocity and enhanced crack arrest toughness for nanocomposites than the virgin polyester.

Note that much of the published research to date on fracture behavior of particulate composites (nano- or micro-) has been performed quasi-statically and very limited data exists from the perspective of dynamic crack growth caused by rapid loading. This gap needs to be bridged if nanocomposites are to find engineering applications such as aerospace and automotive structures, sporting equipment, and high speed trains where stress-wave loading occurs. Further, with regard to particle size, the aforementioned fracture works essentially suggest a need for comparatively studying nano- and micron-size filled composites particularly under rapid loading conditions. Thus, in this research the effects of particle size-scale (nano- vs. micro-) and filler volume fraction on the fracture behavior of particulate composites are experimentally investigated under both quasi-static and stress-wave dominant loading conditions. In the following section, the details of material preparation, characterization, and specimen geometry are provided. Next, the basic concept and the approach of the optical methodology, the experimental setup and testing procedure used in this research are briefly described. This is followed by a detailed description of experimental results in a comparative manner for all categories of specimens in terms of load–deflection responses, quasi-static fracture toughness, dynamic fracture parameters such as crack velocity histories, mode-I SIF histories, K_I^d–V relationships. Subsequently, the results are supported qualitatively and quantitatively by microscopic examination of fractured surfaces and roughness measurements. Lastly, the major conclusions of this work are discussed and summarized.

2. Materials processing and characterization

2.1. Materials

Two sizes of spherical rigid fillers, one nano-sized silica particles of average diameter 20 nm (Nanopox F400 from Nanoresins, Germany) and the other micron-sized glass particles of mean diameter 35 μm (Spheriglass®, Potters Industries Inc.) were used in this study.[1] The Nanopox F400 consisted of 40 wt.% (~26 vol.% [10,19]) silica nanoparticles supplied as colloidal silica gel in a diglycidyl ether of bis-phenol A (DGEBA) resin whereas the micro-filler particles were received in powder form. A low viscosity epoxy system (Epo-Thin™ from Beuhler, Inc. USA) consisting of DGEBA resin and an amine-based hardener in the ratio of 100:39 was employed as the matrix material. This epoxy system offers low shrinkage and relatively long duration room temperature curing characteristics.

2.2. Particulate composites preparation

Prior to mixing the constituents, each type of filler was preheated in an oven at 70 °C for an hour in order to release any

[1] The choice of the latter was based on the previous study [28] that offered the largest gain in dynamic fracture toughness under dynamic loading conditions.

trapped moisture and then cooled gradually to ambient temperature. The nanocomposites and the micron-size particle filled composites were loaded with 3%, 5%, 7%, and 10% of fillers (by volume). Care was exercised to ensure uniform distribution of each type of filler throughout the matrix. It should be noted that the Nanopox F400 resin pre-loaded with silica nanoparticles was diluted first by the required amount of DGEBA resin in such a way that the end product had the appropriate content of nanosilica for the desired volume fraction. The material was mixed using a magnetic stirrer for 20 min at 50 °C to obtain a homogenous mixture. While the mixture remained at a relatively low viscosity at 50 °C, degassing was done every 30 min for 2 h to remove any trapped bubbles generated during mixing. This ensured full degassing of the mixture. This also allowed sufficient time for the mixture to reach room temperature. After degassing, the stoichiometric amount of the hardener was added to the mixture, which was again magnetically stirred for 5 min and degassed for 20 min. The mixture was then poured into molds coated with a release-agent. For the preparation of micro-particle filled composites, the predetermined amounts of filler particle volume fractions were added into DGEBA epoxy resin followed by mixing and degassing steps as mentioned above. However, in this case, after mixing of hardener and degassing, the mixture was continuously stirred until the mixture showed a tendency to gel before pouring into molds. This helped to eliminate sedimentation of the filler particles during subsequent curing. The poured mixtures were allowed to cure for 96 h at room temperature. The cured sheets were removed from the molds and further rested for a week prior to machining and testing.

2.3. Microstructural characterization

Microscopic studies were done to get an insight of the quality of exfoliation of filler particles into epoxy matrix. The particle distribution in nano- and micro-particle filled composites was examined using transmission electron microscope (TEM) and optical microscope, respectively. In the case of nanocomposites, thin film slices (80–90 nm thick) for TEM were microtomed using Leica UltraCut T Microtome. These slices were then mounted on carbon-filmed copper grids and the associated through-thickness morphologies were viewed using a ZEISS EM10 transmission electron microscope at an accelerating voltage of 70 kV. For micron-size particulate composites, samples with cross-sectional area 15 mm × 8 mm were cut and polished sequentially using 600, 1000 and 2000 grit wet emery papers. The polished surfaces of these samples were viewed using Nikon Eclipse L150 optical microscope.

Fig. 1 shows micrographs depicting particle distribution in nano- and micro-particle filled composites. It can be seen that particle agglomeration is absent in all micrographs. The TEM images in Fig. 1a and b show a very uniform distribution of nanoparticles throughout the epoxy matrix with 3% and 10% V_f, respectively. Note that the bigger and darker spots in the TEM images indicate overlapping of two or more particles in the thickness direction. *As noted earlier, the TEM specimens were ~90 nm thick, and hence, the apparent volume fraction of nanoparticles is higher than the true volume fraction.* The optical images in Fig. 1c and d show well-dispersed micro-particles with 3% and 10% V_f, respectively. It should be noted that unlike TEM images the optical micrographs show particle distribution imaged only at zero thickness. The dark spots in these micrographs are debris due to polishing and the dark lines are scratch marks.

2.4. Elastic characterization

The elastic and physical characteristics of filled composites as a function of volume fraction of the dispersant were determined by indirect means of ultrasonic pulse-echo measurement at several

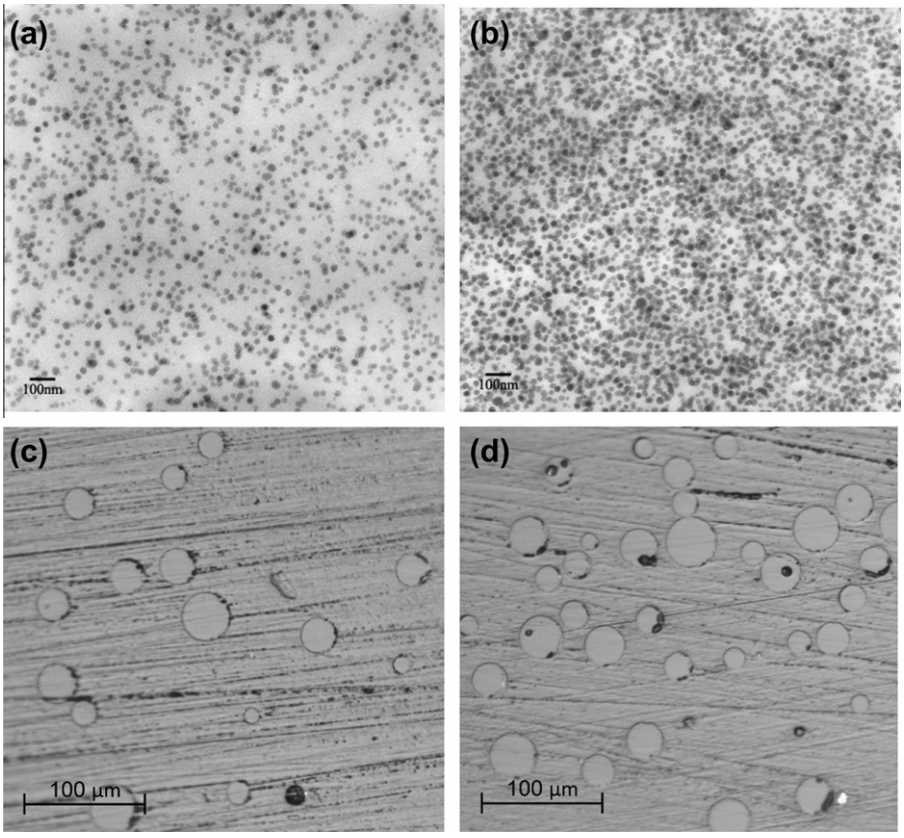

Fig. 1. Micrographs showing particle dispersion: (a) TEM image of 3% V_f nano-filler. (b) TEM image of 10% V_f nano-filler. (c) Optical micrograph of 3% V_f micro-filler. (d) Optical micrograph of 10% V_f micro-filler.

discrete locations of the cured sheets. The longitudinal (C_L) and shear (C_S) wave speeds were determined by measuring transit time for the pulse to travel twice the thickness of the sample using 10 and 5 MHz transducers (Panametric, Inc.), respectively. The mass density, ρ, of each composition was also determined. The values of dynamic elastic modulus (E_d) and Poisson's ratio (v_d) were then calculated using measured wave speeds and mass density from,

$$C_L = \sqrt{\frac{E_d(1-v_d)}{\rho(1+v_d)(1-2v_d)}}, \quad C_S = \sqrt{\frac{E_d}{2\rho(1+v_d)}}. \tag{1}$$

The measured elastic and physical properties of nano- and micro-particle filled-composites are shown in Tables 1 and 2, respectively. The effect of particle volume fraction on measured properties is quite evident. It can be seen that in both types of filled-composites, as the particle volume fraction increases, the density, longitudinal and shear wave speeds, and elastic modulus increase in a monotonic fashion with a negligible change in the Poisson's ratio. It should be noted here that for any given volume fraction (3%, 5%, 7%, 10%), the particle size-scale (nano- vs. micro-) does not affect the elastic and physical characteristics. That is, the values of each measured property are the same for both nano- and micro-filler cases within the measurement error.

2.5. Specimen fabrication and geometry

The cured composite sheets were machined into rectangular coupons of nominal dimensions 106 mm × 20 mm × 8 mm for quasi-static fracture tests (span 90 mm) and 212 mm × 50 mm × 8 mm for dynamic fracture experiments (span 196 mm). An edge notch of 4 mm and 10 mm in length was first cut using a diamond impregnated circular saw (thickness ~300 μm) into the samples for quasi-static and dynamic fracture tests, respectively. The notch tip was then sharpened using a fresh razor blade for each specimen in order to have a naturally sharp crack-tip to achieve a consistent crack initiation followed by a steady growth [32].

The dynamic fracture experiments were performed using the method of digital image correlation (DIC) to quantify crack-tip deformations and hence the crack growth parameters. (The details of this method are provided in Section 3.2.) Hence, a random speckle pattern was created on the surface of the sample by spraying a fine mist of black and white paints alternatively. Fig. 2 depicts the specimen geometry, dimensions and loading configuration along with crack-tip coordinate system and an illustration of random speckle pattern. The region in the dotted box represents 30 × 30 mm^2 region-of-interest.

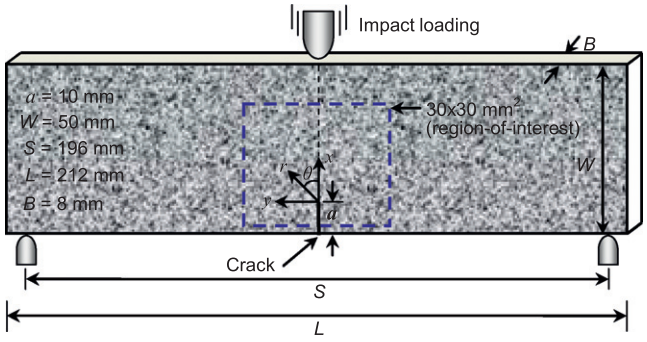

Fig. 2. Dynamic fracture specimen geometry with crack-tip coordinate system and loading configuration, with an illustration of random speckle pattern.

3. Experimental details

3.1. Quasi-static fracture tests

Symmetric three-point bending tests were conducted to measure quasi-static fracture toughness, K_{Ic}, in accordance with ASTM D5045 guidelines [33]. The single-edge-notched bend, SENB, specimens were loaded in a displacement-controlled mode at a cross-head speed of 0.254 mm/min using Instron 4465 testing machine. Typically, four experiments were conducted at each volume fraction. The load vs. deflection data was recorded up to complete fracture of the specimens and K_{Ic} was calculated using the load at fracture. The K_{Ic} value was computed using Eq. (2) [34],

$$K_{Ic} = \frac{3\frac{PS}{BW^2}\sqrt{a}}{2\left(1+2\frac{a}{W}\right)\left(1-\frac{a}{W}\right)^{3/2}} \times \left[1.99 - \frac{a}{W}\left(1-\frac{a}{W}\right)\left\{2.15 - 3.93\left(\frac{a}{W}\right) + 2.7\left(\frac{a}{W}\right)^2\right\}\right] \tag{2}$$

where P, S, B, W and a are the load at fracture, the span, the thickness, the width and the crack length of the specimen, respectively.

3.2. Dynamic fracture tests

3.2.1. Experimental approach

The dynamic fracture behavior was studied using 2D digital image correlation (DIC) method. In this method, the decorated random speckle patterns on a specimen surface were monitored during a fracture event. The speckle patterns were recorded before and after deformation. The images from the deformed and undeformed

Table 1
Measured dynamic material properties of nano-particle filled epoxies at different volume fraction (V_f).

V_f (%)	Density, ρ (kg/m^3)	Longitudinal wave speed, C_L (m/s)	Shear wave speed, C_S (m/s)	Dynamic elastic modulus, E_d (GPa)	Poisson's ratio, v_d	Impedance, $\rho.C_L$ (MPa s/m)
0	1124	2487	1136	3.97	0.368	2.80
3	1156	2547	1188	4.44	0.360	2.94
5	1181	2577	1233	4.85	0.352	3.04
7	1218	2604	1250	5.14	0.350	3.17
10	1272	2634	1268	5.52	0.348	3.35

Table 2
Measured dynamic material properties of micro-particle filled epoxies at different volume fraction (V_f).

V_f (%)	Density, ρ (kg/m^3)	Longitudinal wave speed, C_L (m/s)	Shear wave speed, C_S (m/s)	Dynamic elastic modulus, E_d (GPa)	Poisson's ratio, v_d	Impedance, $\rho.C_L$ (MPa s/m)
3	1151	2543	1194	4.46	0.359	2.93
5	1184	2569	1216	4.76	0.356	3.04
7	1223	2591	1239	5.08	0.352	3.17
10	1279	2627	1257	5.46	0.351	3.36

sets were paired and analyzed using image correlation methodology. Conceptually, a sub-image in an undeformed image was selected and its location in the corresponding deformed image was searched to find its local displacements. In this study, an approach developed [35–37] on a MATLAB™ platform was used to estimate in-plane surface displacement components. In the first step, displacements were estimated by performing a 2D cross-correlation of gray scales in the Fourier domain and the peak of the correlation function detected to a sub-pixel accuracy using bicubic interpolation. This process was repeated for the entire image to obtain full-field in-plane displacements. In the second step, an iterative approach based on nonlinear least-squares minimization was used to minimize the 2D cross-correlation function in the spatial domain to refine the previously computed displacements as initial guess. Further details are avoided here for brevity.

3.2.2. Experimental setup and testing procedure

The schematic of the experimental set-up used is shown in Fig. 3. It included a drop-tower (Instron-Dynatup 9250HV, USA) for impact loading the specimens and a Cordin 550 ultra high-speed digital framing camera (Cordin Scientific Imaging, USA) for recording speckle images during the fracture event. The drop-tower was equipped with an instrumented tup (hemispherical profile) and a pair of instrumented anvils for recording force and support reaction histories, respectively. The set-up also included instrumentation to produce a delayed trigger pulse when the impactor contacted the specimen ($t = 0$). Two high-energy flash lamps, triggered by the camera and a pulse generator, were employed to illuminate the sample surface. Also, two separate computers, one to record the impact force and anvil reaction histories, and the other to control the high-speed camera and to store the images were used. The light intensity from the specimen surface in the region of interest was recorded.

The Cordin 550 ultra high-speed digital framing camera is capable of recording images on 32 individual 1000×1000 pixel (pixel size: 7.4 μm square) CCD sensor array positioned circumferentially around a five-facet rotating mirror which reflects and sweeps light over these sensors. Additional details about the camera performance evaluation and optical calibration can be found in Refs. [35–37]. The specimen decorated with random speckles was initially rested on two instrumented anvils and the camera was focused on a $30 \times 30\,\text{mm}^2$ region-of-interest in the crack-tip vicinity. Prior to impacting the specimen, a set of 32 images were recorded at a chosen framing rate. While keeping all camera settings same, a second set of 32 images was captured when the specimen was impacted at a velocity of 4.5 m/s. In order to capture the entire fracture event, the images in the case of micro-particle filled composites were recorded at a framing rate of 250,000 frames per second whereas framing rates ranging from 250,000–300,000 frames per second were used for nanocomposite specimens. A total of 32 images were recorded for undeformed and deformed sets. The corresponding two images of each sensor were paired from undeformed and deformed sets and analyzed.

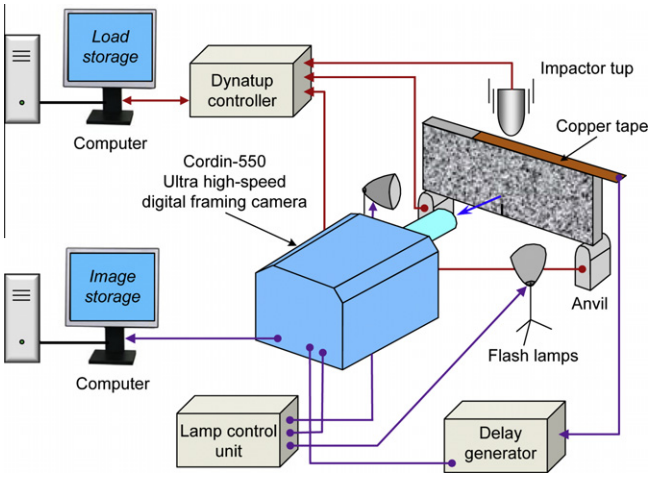

Fig. 3. Schematic of the experimental setup for dynamic fracture study.

3.2.3. Image analysis details

As noted earlier, the recorded speckle images corresponded to a $30 \times 30\,\text{mm}^2$ region on the specimen surface. The size of the decorated speckles and the optical magnification used were such that each speckle occupied 4–6 pixels on the image plane. Care was also exercised regarding electronic gain setting of the high-speed camera sensors and intensity of the flash lamps to produce a near Gaussian distribution of gray scales for each image in the mid-range of 0–255 (8 bit) intensities. That is, saturation or underexposure of pixels was avoided by trial and error prior to carrying out the actual experiment. Each resulting image was segmented into sub-images consisting of 26×26 pixels for analysis. While analyzing images, no overlapping of sub-images was used. This resulted in 37×37 matrix of data points in the region-of-interest.

3.2.4. Evaluation of crack velocity and stress intensity factors (SIFs)

The position of the current crack-tip from each digitized image was used to measure the instantaneous values of crack length. However, the presence of digitizing errors often manifests in the crack extension data. To minimize this error, the crack length data at an instant i was smoothed using a quadratic Bézier curve [38],

$$a_i(s) = (1-s)^2 d_i + 2s(1-s)d_{i+1} + s^2 d_{i+2}, \quad 0 \leqslant s \leqslant 1 \tag{3}$$

where s, d and a are the smoothing parameter, the digitized data, and the smoothed crack length data, respectively. In the above expression d_i, d_{i+1}, d_{i+2} are the control points of $a_i(s)$. A smoothing parameter of 0.5 was chosen so that the smoothed data point is located at midway from a data point to an adjacent point. Subsequently, the crack velocity (V) was estimated from the smoothed crack length histories using forward difference method,

$$V_i = \left(\frac{da}{dt}\right)_i = \frac{a_{i+1} - a_i}{t_{i+1} - t_i} \tag{4}$$

where a and t are crack length and time, respectively, at a given instant i.

The mode-I and mode-II stress intensity factors (SIFs) were evaluated using an over-deterministic least-squares analysis of crack-opening and crack-sliding displacements, respectively. The governing asymptotic expressions for crack-opening (v) and crack-sliding (u) displacement fields near the tip of a dynamically loaded stationary crack are expressed as follows:

$$\begin{Bmatrix} u(r,\theta) \\ v(r,\theta) \end{Bmatrix} = \sum_{n=1}^{\infty} \frac{(K_I^d)_n}{2\mu} \frac{r^{n/2}}{\sqrt{2\pi}} \times \begin{Bmatrix} \kappa \cos\frac{n}{2}\theta - \frac{n}{2}\cos\left(\frac{n}{2}-2\right)\theta + \left\{\frac{n}{2} + (-1)^n\right\}\cos\frac{n}{2}\theta \\ \kappa \sin\frac{n}{2}\theta + \frac{n}{2}\sin\left(\frac{n}{2}-2\right)\theta - \left\{\frac{n}{2} + (-1)^n\right\}\sin\frac{n}{2}\theta \end{Bmatrix} + \sum_{n=1}^{\infty} \frac{(K_{II}^d)_n}{2\mu} \frac{r^{n/2}}{\sqrt{2\pi}} \times \begin{Bmatrix} \kappa \sin\frac{n}{2}\theta - \frac{n}{2}\sin(\frac{n}{2}-2)\theta + \left\{\frac{n}{2} - (-1)^n\right\}\sin\frac{n}{2}\theta \\ -\kappa \cos\frac{n}{2}\theta - \frac{n}{2}\cos\left(\frac{n}{2}-2\right)\theta + \left\{\frac{n}{2} - (-1)^n\right\}\cos\frac{n}{2}\theta \end{Bmatrix} \tag{5}$$

where r and θ are the polar coordinates defined at the current crack-tip, κ is $(3 - \nu_d)/(1 + \nu_d)$ for plane stress where ν_d is the Poisson's

ratio and μ is the shear modulus. In the above expressions, the coefficients $(K_I^d)_n$ and $(K_{II}^d)_n$ of the dominant terms ($n = 1$) are the so-called mode-I and mode-II dynamic SIFs, respectively. The above in-plane displacement fields implicitly assume that the inertia effects are accounted for by the coefficients while maintaining the functional form of the quasi-static counterpart. However, when the crack initiates, the in-plane displacement components v and u for a steadily growing crack are given by [39]:

$$\begin{Bmatrix} u(r,\theta) \\ v(r,\theta) \end{Bmatrix} = \sum_{n=1}^{\infty} \frac{(K_I^d)_n B_I(V)}{2\mu}\sqrt{\frac{2}{\pi}}(n+1) \times \begin{Bmatrix} r_1^{n/2}\cos\frac{n}{2}\theta_1 - h(n) r_2^{n/2}\cos\frac{n}{2}\theta_2 \\ -\beta_1 r_1^{n/2}\sin\frac{n}{2}\theta_1 + \frac{h(n)}{\beta_2} r_2^{n/2}\sin\frac{n}{2}\theta_2 \end{Bmatrix} + \sum_{n=1}^{\infty} \frac{(K_{II}^d)_n B_{II}(V)}{2\mu}\sqrt{\frac{2}{\pi}}(n+1) \times \begin{Bmatrix} r_1^{n/2}\sin\frac{n}{2}\theta_1 - h(\bar{n}) r_2^{n/2}\sin\frac{n}{2}\theta_2 \\ \beta_1 r_1^{n/2}\cos\frac{n}{2}\theta_1 + \frac{h(\bar{n})}{\beta_2} r_2^{n/2}\cos\frac{n}{2}\theta_2 \end{Bmatrix} \quad (6)$$

where

$$r_m = \sqrt{x^2 + \beta_m^2 y^2},\ \theta_m = \tan^{-1}(\beta_m y/x), m = 1,2,$$
$$\beta_1 = \sqrt{1-(V/C_L)^2},\ \beta_2 = \sqrt{1-(V/C_S)^2}$$

$$C_L = \sqrt{\frac{(\kappa+1)\mu}{(\kappa-1)\rho}}, C_S = \sqrt{\frac{\mu}{\rho}}, \kappa = \begin{cases} (3-\nu)/(1+\nu_d) : \text{plane stress} \\ (3-4\nu_d) : \text{plane strain} \end{cases}$$

$$h(n) = \begin{cases} 2\beta_1\beta_2/(1+\beta_2^2) : n \text{ odd} \\ (1+\beta_2^2)/2 : n \text{ even} \end{cases} \quad \text{and} \quad h(\bar{n}) = h(n+1)$$

$$B_I(V) = \frac{(1+\beta_2^2)}{D},\ B_{II}(V) = \frac{2\beta_2}{D},\ D = 4\beta_1\beta_2 - (1+\beta_2^2)^2. \quad (7)$$

In the above equations, (x, y) and (r, θ) are the instantaneous Cartesian and polar coordinates, respectively, aligned at the current crack-tip, V is the crack-tip velocity, C_L and C_S are homogenized longitudinal and shear wave speeds of the material, ρ is the mass density, μ and ν_d are the shear modulus and the Poisson's ratio, respectively. Again, the coefficients $(K_I^d)_n$ and $(K_{II}^d)_n$ of the dominant terms ($n = 1$) are the mode-I and mode-II dynamic SIFs respectively. Further, Eq. (6) can be reduced to the form of a dynamically loaded stationary crack in the limit the crack velocity $V \to 0$.

In order to extract SIF history, the crack-opening and crack-sliding displacement fields were digitized by identifying the current crack-tip location in the image. The displacement data used in the analysis was collected in the vicinity of the crack-tip and limited to the region $0.4 < r/B < 1.5$ and ($-150° \le \theta \le -90°$ and $90° \le \theta \le 150°$) to minimize 3D effects on least-squares analysis [40]. At each data point, v and u displacement values as well as the location of these points were stored. The digitized data were used in Eqs. (5) and (6) along with an over-deterministic least-squares analysis scheme to estimate the SIFs. This process was carried out for all image pairs and the SIF histories were generated.

4. Results

4.1. Experimental repeatability

In order to verify repeatability in fracture behaviors and measurements, multiple experiments were performed for both nano- and micro-filler composites under quasi-static and dynamic loading conditions. Fig. 4a and b show results for multiple quasi-statically fractured specimens. An excellent repeatability in load–deflection responses of four specimens can be seen at 10% volume fraction for each category. At this volume fraction, the nanocomposite specimens fractured at a peak load of 1158 ± 45 N, whereas the specimens with micro-filler failed at 687 ± 12 N. A noticeable departure from linearity of global load–deflection response close to fracture is evident in Fig. 4a whereas the plots remain linear in Fig. 4b up to fracture.

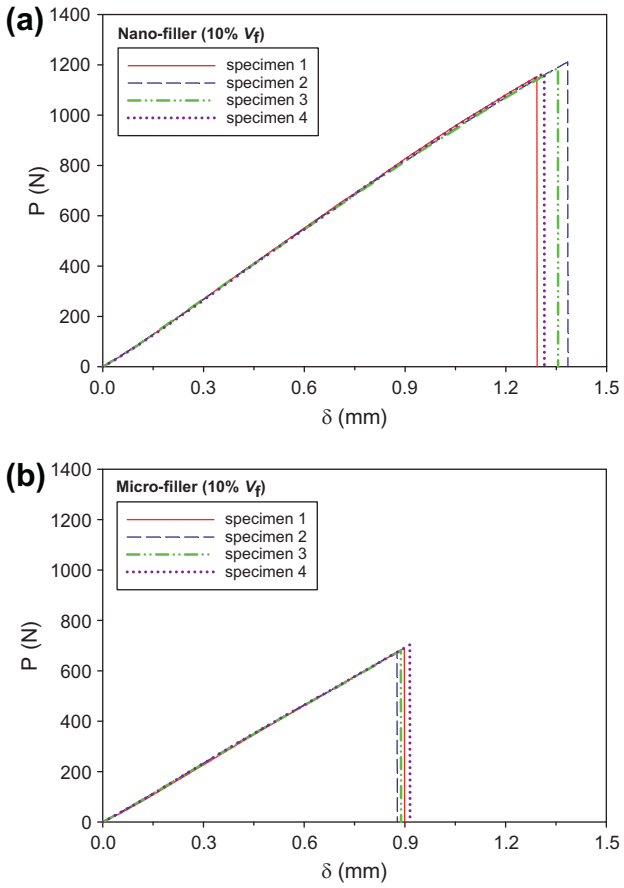

Fig. 4. Experimental repeatability in quasi-static fracture tests: (a) Load–deflection response of 10% V_f nano-filler modified epoxy. (b) Load–deflection response of 10% V_f micro-filler modified epoxy.

Figs. 5–7 show repeatability in dynamic fracture behavior in terms of crack velocity, mode-I SIF and load histories at 10% V_f for nano- as well as micro-filler composites. Fig. 5a and b depict repeatability in crack growth histories in three specimens for each type of filler. Here t_i denotes the time at crack initiation after impact. In all the cases it can be seen that following initiation, crack accelerated and attained a steady state velocity. At 10% V_f, the nano-filler specimens show a steady state velocity of approximately 570 m/s whereas it is about 220 m/s in the micro-filler cases. All the three specimens in each category show good repeatability in crack velocity profiles.

The mode-I SIF, K_I^d histories obtained using the method described earlier for the same three specimens are shown in Fig. 6a and b for nano- as well as micro-filler composites, respectively. The K_I^d at crack initiation is indicated by an arrow for each specimen. For nano-filler specimens the crack initiation (after impact) time range is 113–120 μs whereas for micro-filler ones it is 120–124 μs. From the perspective of dynamic fracture experiments, it is important to note that the K_I^d profiles show excellent repeatability of the entire fracture event for each type of filler. Again, for both

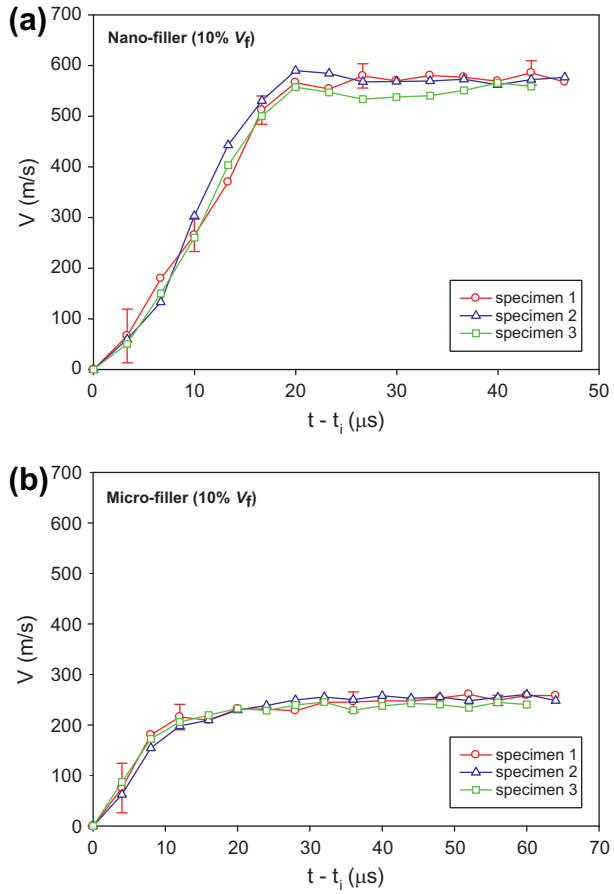

Fig. 5. Experimental repeatability in dynamic fracture tests: (a) Crack-tip velocity histories of 10% V_f nano-filler modified epoxy. (b) Crack-tip velocity histories of 10% V_f micro-filler modified epoxy.

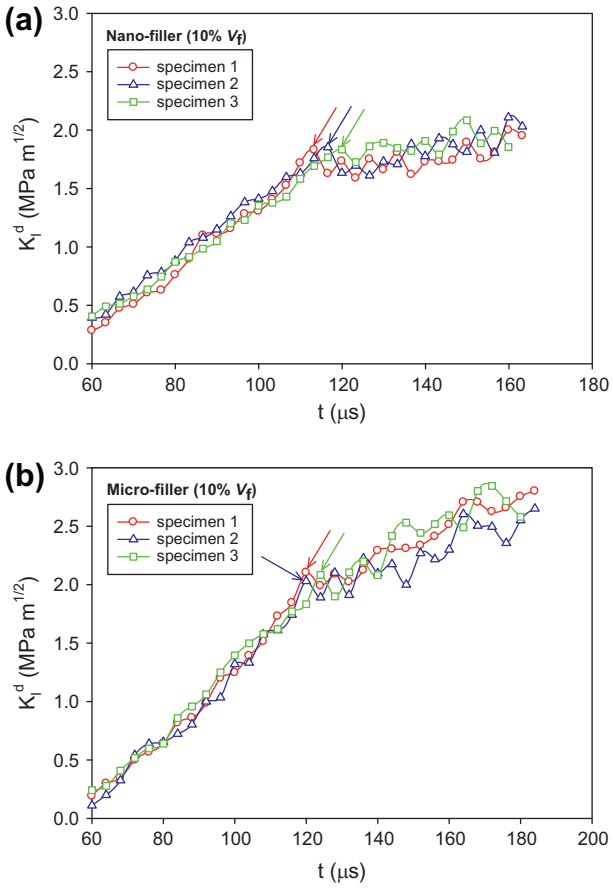

Fig. 6. Experimental repeatability in dynamic fracture tests: (a) Mode-I dynamic SIF histories of 10% V_f nano-filler modified epoxy. (b) Mode-I dynamic SIF histories of 10% V_f micro-filler modified epoxy. The crack-initiation value is indicated by an arrow for each specimen. Note that post-initiation K_I^d values are increasing more slowly in nano-filler case compared to micro-filler counterpart.

types of composites, the SIF increases monotonically up to crack initiation and pre-initiation SIF histories essentially coincide for all three specimens. For nano-filler specimens, the value of K_I^d at initiation is ~1.85 MPa m$^{1/2}$ whereas it is ~2.13 MPa m$^{1/2}$ for micro-filler specimens. Following crack initiation, a noticeable drop in K_I^d can be seen in each specimen for both filler categories due to unloading near the initial notch tip. This is followed by a gradual increase in K_I^d until the fracture is complete for both filler types. The rise in post-initiation K_I^d values is smaller in the nano-particle filled epoxy ($dK_I^d/dt \sim 5.3 \times 10^3$ MPa m$^{1/2}/s$) when compared to the micron-size filler counterpart ($dK_I^d/dt \sim 13 \times 10^3$ MPa $m^{1/2}/s$).

The tup and anvil load histories were recorded for each experiment and are shown in Fig. 7a and b for the three nano- and micro-particle filled specimens with 10% V_f, respectively. In these plots, again an excellent repeatability in tup load as well as in left and right support reaction histories is quite evident for all three specimens. In these experiments, the complete fracture of the specimen occurred within ~200 μs after impact. Thus, only the dominant first peak of the tup load history is significant. Note that the peak impact force (compressive) recorded by the tup in case of micro-filler specimens is slightly higher than the nano-filler counterparts, suggesting the role of particle size. It can also be seen that supports register the reaction force only after ~300 μs by which time the crack had already traversed the specimen width. This shows that reaction forces from support anvils do not contribute to the crack initiation and crack growth in the specimens, suggesting that a free-free cracked beam should suffice analytical or computational modeling of these experiments.

4.2. Quasi-static fracture behavior

The quasi-static fracture test results are summarized in Figs. 8 and 9. The load vs. deflection responses at different volume fractions are plotted in Fig. 8a and b for nano- and micro-filler epoxies, respectively. It can be seen that for both filler loadings, the load rises linearly (except 7% and 10% V_f nanocomposites showing noticeable nonlinearity prior to fracture) up to a point at which abrupt crack growth ensues causing a sudden drop in the load. It can also be observed that the peak loads and the corresponding load-point deflections show increasing trends, suggesting that the work needed for crack initiation (area under the load–deflection curve), increases with filler volume fraction. Further, note that in both types of fillers the stiffness of the filled-composites generally increase with filler volume fraction. Moreover, for any given volume fraction the nano-filler specimens sustained higher loads as well as deflections up to failure when compared to micro-filler counterparts.

The quasi-static fracture toughness, K_{Ic}, measured at the onset of crack growth in each case and the variation of K_{Ic} as a function of volume fraction of nano- and micro-fillers is plotted in Fig. 9. Each data point represents an average of four measured values of K_{Ic} and the error bars indicate their standard deviations. For both types of filler loadings, the fracture toughness increases relative to neat epoxy as V_f increases. The observed trends in K_{Ic} for both types of filler loadings are in agreement with previous works on micro-particle filled [2–5] and nanosilica filled [12–17] epoxies.

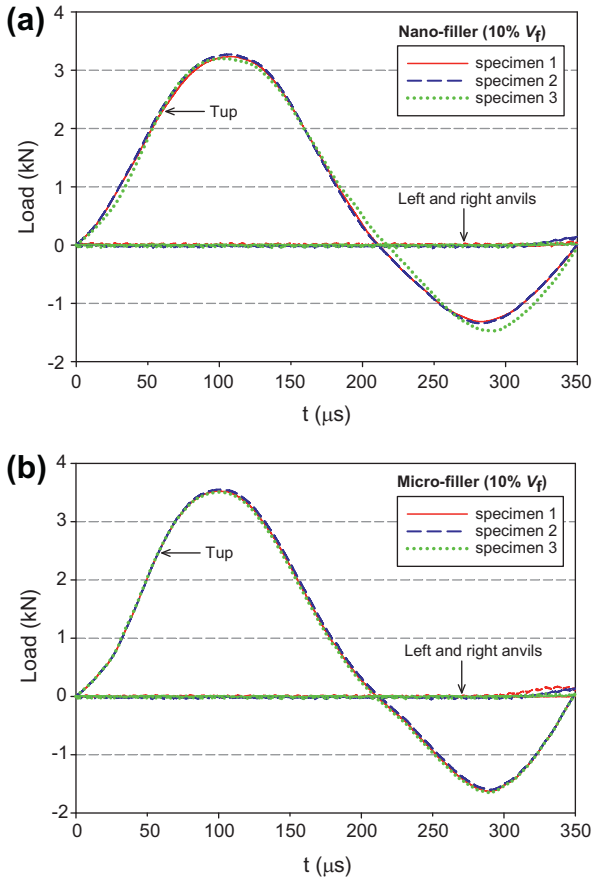

Fig. 7. Experimental repeatability of load histories for dynamic fracture tests: (a) 10% V_f nano-particle filled epoxy. (b) 10% V_f micro-particle filled epoxy. (Note that the tup loads are plotted as positive values for compression.)

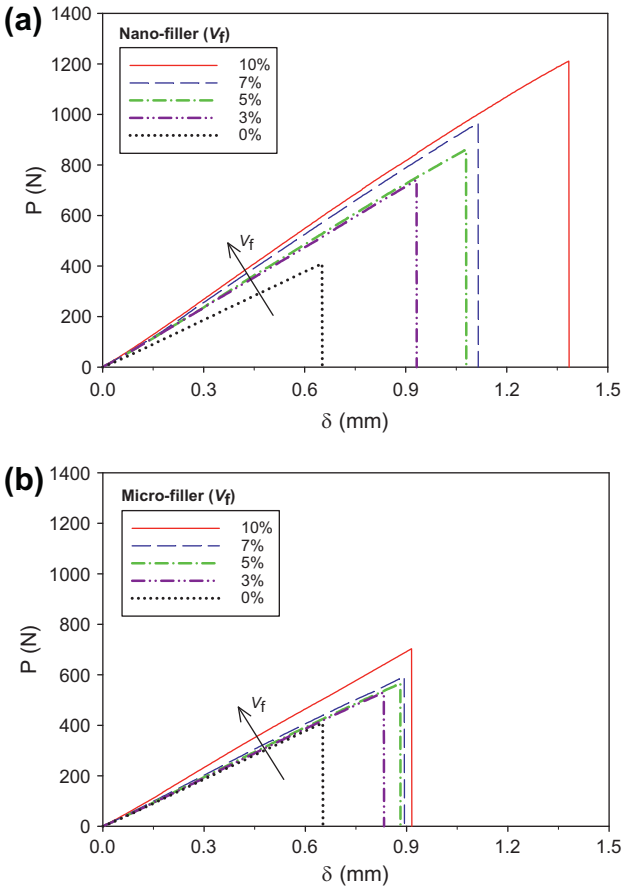

Fig. 8. Load–deflection response for quasi-static fracture tests at different volume fractions: (a) Nano-filler modified epoxies. (b) Micro-filler modified epoxies.

Fig. 9 also shows that the fracture toughness of nano-particle filled specimens increases dramatically with volume fraction relative to the micro-filler counterparts. Furthermore, the enhancement in K_{Ic} is significantly higher than the micro-filler cases for any given volume fraction. For example, a ~42% and ~78% enhancement in K_{Ic} values at 5% and 10% volume fraction, respectively, for nano-sized filler relative to micro-filler case is evident.

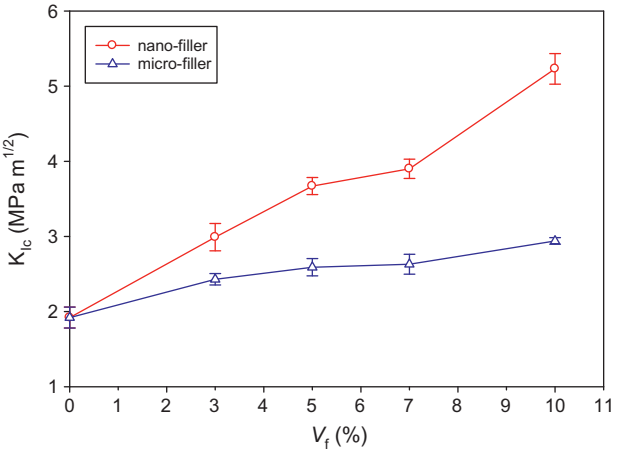

Fig. 9. Variation of quasi-static fracture toughness (K_{Ic}) with filler volume fraction (V_f) for nano- and micro-filler modified epoxies.

4.3. Dynamic fracture response

4.3.1. Surface deformation histories

A sequential arrangement of a few selected speckle images of 30×30 mm^2 region-of-interest where surface deformations were monitored optically during the dynamic fracture of specimens with 10% volume fraction for nano- and micro-filler cases is shown in Fig. 10. The first and second rows of speckle images are for nano- and micro-filler specimens, respectively. The specimens were subjected to symmetric impact loading and the initial notch as well as the sharp growing crack is visible. The time instant (t) after impact at which the images were recorded is also shown and the current crack-tip is indicated by an arrow. In order to compare the effect of particle size-scale on the extent of crack growth, the speckle images in each column for nano- and micro-fillers are shown here for nearly same time instants. It can be seen that at approximately same time instant, crack propagation in the nano-filler specimen is more than the micro-filler counterpart. Further, the crack extension is about twice in the former compared to the latter.

As described earlier, a sub-image size of 26×26 pixels was chosen for image correlation analysis and displacements fields were obtained as 37×37 data points for each pair. Subsequently, full-field in-plane displacement contours with 5 μm per contour interval were generated. A few representative speckle images with corresponding crack-opening (v-field or displacement along the y-axis) and crack-sliding (u-field or displacement along the x-axis) displacement contours for nano-filler (10% V_f), micro-filler (10% V_f) and neat epoxy specimens are presented in Fig. 11. Here, at a particular time instant, $t \sim 160$ μs, crack extension in nano-filler specimen is larger than neat epoxy and micro-filler specimens,

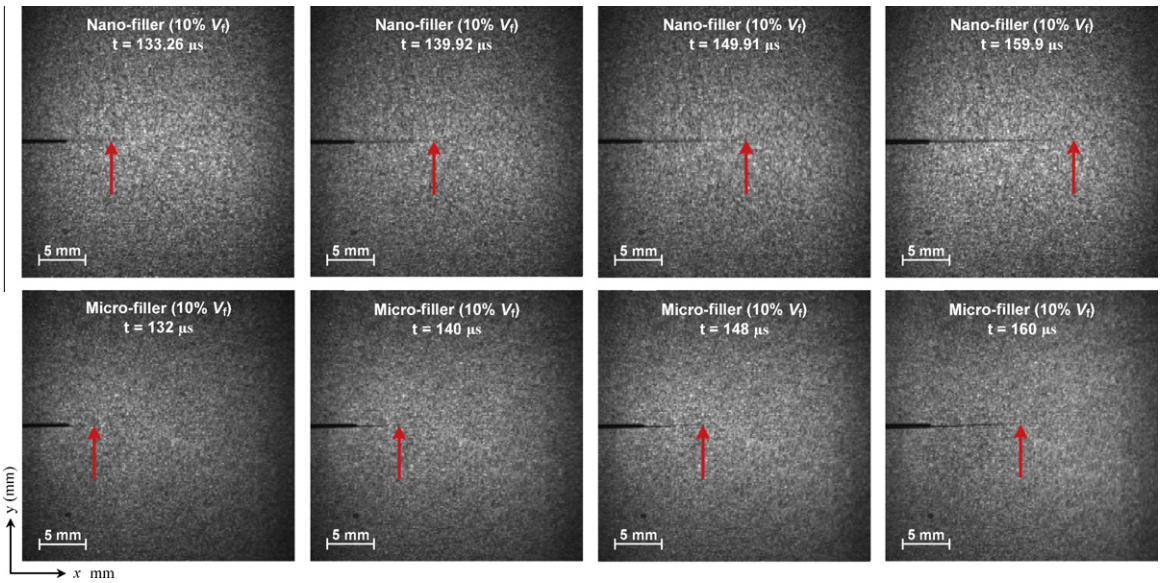

Fig. 10. Few selected speckle images of nano- and micro-filler modified epoxy specimens with 10% V_f at approximately same time instants. Each image represents 30×30 mm^2 region-of-interest recorded by the high-speed digital framing camera at framing rates of 300,000 and 250,000 frames per second for nano- and micro-filler modified epoxies, respectively. The moving crack-tip is indicated by an arrow and the dark line is the initial crack in the photographed images.

whereas the slowest crack growth is evident in the micro-filler specimen. The v- and u-fields show that contour lines and magnitude of displacement (in μm shown by color-bars) are nearly symmetric relative to the crack path suggesting dominant mode-I fracture. The contour lines in the u-field show a set of isolines emerging from right-hand side of the contour plots due to impact loading on the edge of the specimen facing the initial crack-tip.

4.3.2. Crack-tip velocity histories

The crack-tip velocity histories were estimated from the smoothed values of instantaneous crack extension data for nano- and micro-filler cases for different volume fractions and are shown in Fig. 12a and b, respectively. It can be seen that following initiation the crack accelerated to a maximum value followed by a modest oscillatory behavior due to the transient nature of impact induced fracture. For nano-particle filled epoxies, as shown in Fig. 12a, the crack-tip velocity shows increasing steady state values as the particle volume fraction increases and the crack propagates at an average velocity of approximately 300, 370, 400, 490, 570 m/s for 0% (neat epoxy), 3%, 5%, 7%, 10% V_f cases, respectively. On the other hand, the velocity trends are the opposite in micro-particle filled epoxies as shown in Fig. 12b. It can be noticed that the average crack velocity decreases slightly as the volume fraction of micron-size particles increases. The effect of particle size-scale on the crack-tip velocity can be consistently compared by plotting crack velocity histories for each volume fraction separately and two representative cases for 5% and 10% V_f are shown in Fig. 13a and b, respectively. The average crack-tip velocities in the nanocomposites are approximately 60%, 160% higher than that observed in the micro-filler cases for 5%, 10% volume fractions, respectively.

4.3.3. Stress intensity factor (SIF) histories

The optically measured mode-I SIF histories for specimens with nano- and micro-fillers at various volume fractions are shown in Fig. 14a and b, respectively. In these plots, the crack-initiation time is denoted by $t - t_i = 0$ μs so that the negative and positive values correspond to the pre-initiation and post-initiation periods, respectively. The pre-initiation data for each specimen in both types of fillers show that the mode-I dynamic SIF, K_I^d, increases gradually until it reaches a threshold value for crack-initiation. Furthermore, the K_I^d values in the pre-initiation regime show increasing trends as the particle volume fraction increases in both nano- and micro-filler specimens. Following initiation, a distinct drop in K_I^d is evident in all specimens (nano- and micro-filler) and it increases subsequently in a nearly steady-state fashion.

For clarity, consistency, and to avoid data clutter, the mode-I SIF behavior for nano- and micro-fillers cases can be systematically compared by plotting SIF histories for two representative cases of 5% and 10% V_f, as shown in Fig. 15a and b. These plots clearly reflect the effect of particle size (nano- vs. micro-) on the dynamic fracture toughness of particulate composites at crack-initiation as well as in the pre- and post-initiation regimes. For each volume fraction, it can be seen that in the pre-initiation period, the K_I^d values are in agreement within the measurement accuracy. However, unlike quasi-static counterparts the dynamic crack-initiation toughness values for nanocomposites are lower than the micro-filler counterparts. Also note that the post-initiation K_I^d values for nanocomposites are also lower than the micro-filler cases for the volume fractions shown. Hence, it is noteworthy that, *under identical impact loading conditions, the micro-filler particulate composites outperform nano-filler ones at crack-initiation as well as in the post-initiation regimes.* Further note that these observed trends of K_I^d for nano- and micro-fillers are consistent with crack-tip velocity histories shown in Fig. 13a and b, as it can be seen that the apparent macro scale crack growth is the slowest in micro-filler cases suggesting higher crack growth resistance, resulting in higher apparent K_I^d values.

The quasi-static crack-initiation toughness (K_{Ic}) and dynamic crack-initiation toughness (K_{Ii}^d) values for nano- and micro-filler epoxies are tabulated in Table 3. It can be seen that the fracture behavior for both types of fillers is loading-rate sensitive. For quasi-static loading, nano-filler epoxies show higher crack-initiation toughness than the micro-filler ones and the opposite is seen under dynamic loading conditions.

4.3.4. K_I^d–V relationship

The existence of K_I^d–V relationship as a dynamic material characteristic has been a subject of interest [41–46] in the past few

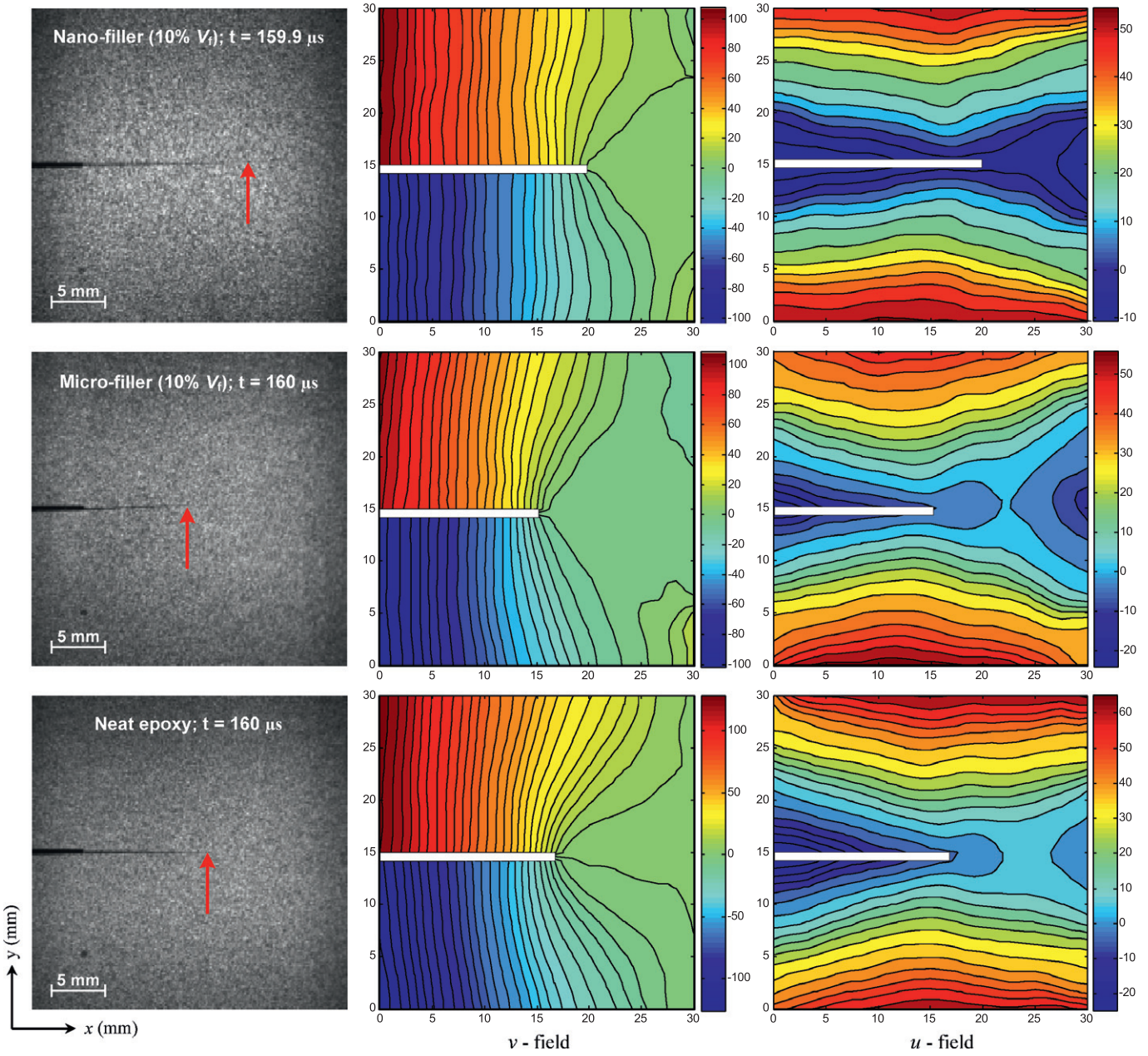

Fig. 11. Representative speckle images of 30 × 30 mm^2 region-of-interest at time instant, $t \sim 160$ μs with corresponding crack-opening (v-field) and crack-sliding (u-field) displacement contours. Contour interval is 5 μm. Color-bars represent displacement in μm. The arrows indicate the current crack-tip position in the speckle images. (For interpretation of the references to color in this figure legend, the reader is referred to the web version of this article.)

decades. Previous studies discuss K_I^d–V characteristics of monolithic materials (neat polymers and steels). In the recent years, the existence of K_I^d–V relations for nanocomposites has been shown in the works of Shukla et al. [29] and Evora et al. [31]. In the present work, the variation of dynamic mode-I SIF with crack-tip velocity for nano- and micro-fillers at 5% and 10% volume fraction as well as for neat epoxy is presented in Fig. 16a and b. These plots show data points after crack-initiation for all experiments performed under identical impact loading conditions. In these plots, at a given volume fraction, both types of fillers exhibit a K_I^d–V variation similar to the previously seen ones in monolithic materials. All the specimens indicate a characteristic near-horizontal tail and near-vertical stem. For each case, in the horizontal portion, a small drop in K_I^d value can be seen. The K_I^d–V profiles also suggest that for each volume fraction, the micro-fillers produce significantly higher crack growth resistance when compared to the ones due to nano-fillers and neat epoxy. The nano-filler specimens show lower K_I^d over a wider range of velocities compared to the micro-filler counterparts and neat epoxy. The terminal velocities in the case of nano-filler specimens are ~400 m/s and ~570 m/s for 5% and 10% volume fractions, respectively, whereas in the case of micro-filler counterparts it is ~250 m/s and ~220 m/s at the same volume fractions, respectively. The K_I^d–V response of neat epoxy in the vertical stem with a terminal velocity of ~300 m/s is, however, bounded by the ones with nano- and micro-filler epoxies. These observations indicate that for the same volume fraction of the filler, nanocomposites fracture at higher crack velocities than the micro-filler and neat epoxy.

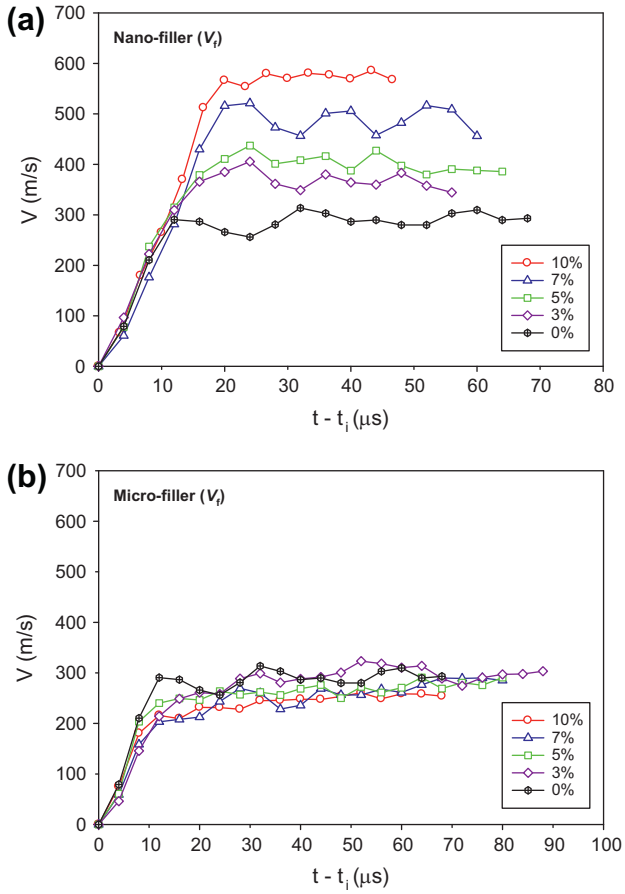

Fig. 12. Crack-tip velocity histories at different volume fractions: (a) Nano-filler modified epoxies. (b) Micro-filler modified epoxies.

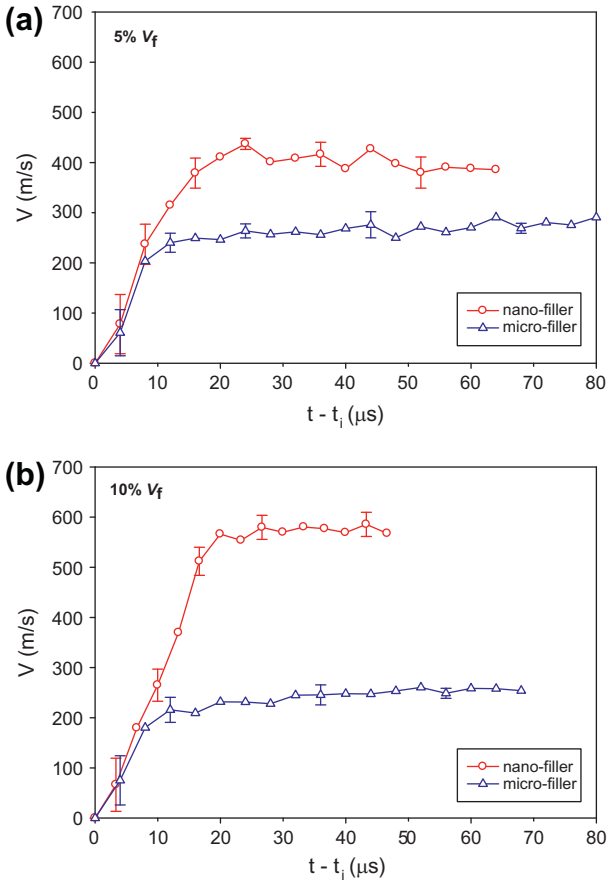

Fig. 13. Role of nano- vs. micro-fillers on crack-tip velocity histories: (a) 5% V_f. (b) 10% V_f.

4.4. Fractography

It has been well recognized that fracture surface topography reveals inherent details of deformation and the associated energy dissipation mechanisms that govern the process of fracture [47–50]. Accordingly, the fracture surfaces were examined both qualitatively and quantitatively. Microscopy was performed for qualitative examination of fracture surfaces of quasi-statically and dynamically failed specimens. Note that the surface features of quasi-statically fractured specimens were evident even to the naked-eye; hence, optical microscope was found suitable for visualizing macro scale surface features. However, finer details were also captured using a scanning electron microscope (SEM) in these cases. For dynamically fractured surfaces, SEM was used since visual inspection was insufficient as the fracture surface features were mainly confined to a very small spatial domain. To further understand fracture surface morphology, roughness measurements were also performed using a Dektak-150 profilometer with a 2 μm stylus for dynamically fractured specimens. The fracture surface profiles were scanned in a stable crack growth zone as shown in the inset of Fig. 19 and will be discussed later in this section. Note that the same region was chosen for SEM analysis of dynamically failed samples.

The optical and SEM micrographs of quasi-statically fractured surfaces of nano- and micro-particle filled epoxies are shown in Fig. 17. The top and bottom row represents micrographs of nano- and micro-filler cases, respectively, for 5% and 10% V_f. The arrow in each optical image indicates initial crack front as well as the direction of crack growth. These optical micrographs can be viewed as a global representation of surface features as the images were captured at low magnification in order to cover maximum region of fractured surfaces. The effect of particle size-scale can be clearly seen on the surface roughness. The optical images of nanocomposites show very rough, highly textured/torn surfaces containing a large number of macro as well as microcracks with deep valleys and furrows with steep ridges. These features markedly amplify with 10% V_f of nano-filler loading. However, similar are absent in optical images of micro-filler counterparts indicating lower quasi-static fracture toughness relative to nanocomposites. Interestingly, three distinct zones-'mirror', 'mist' and 'hackle'-are also quite evident in optical micrographs of nanocomposite specimens. The mirror zone can be clearly identified as a flat and smooth region appearing in the lower central portion of 5% nano-filler case close to the initial crack front, whereas it is at the lower right side of 10% nano-filler loading. In each case, surrounding the mirror zone is the mist region appearing with a slight change in the surface texture. The outwardly expanding roughness markings surrounding the mirror and mist zones can be recognized as hackle regions which are generally associated with the violent stage of fracture in which tremendous amount of fracture energy is dissipated through both plastic deformation and by the generation of additional fracture surfaces. However, these features appear to be less prominent in the case of micro-filler specimens. In Fig. 17, adjacent to each optical image, SEM micrographs of a selected region (the boxed region) is shown. Note that the nanoparticles were hard to detect even at higher magnifications as the nanoparticle size and gold coating layer were of nearly the same order of magnitude. The SEM micrographs for nano-filler cases represent features of the

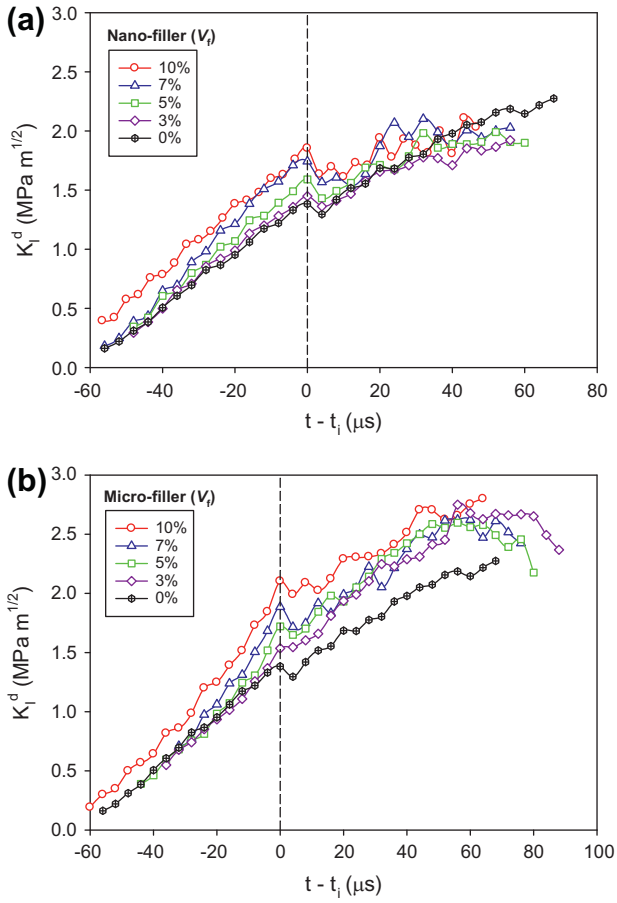

Fig. 14. Mode-I dynamic SIF histories at different volume fractions: (a) Nano-particle filled epoxies. (b) Micro- particle filled epoxies. (Time base is shifted such that $t - t_i = 0$ corresponds to crack-initiation as shown by the vertical dashed line.)

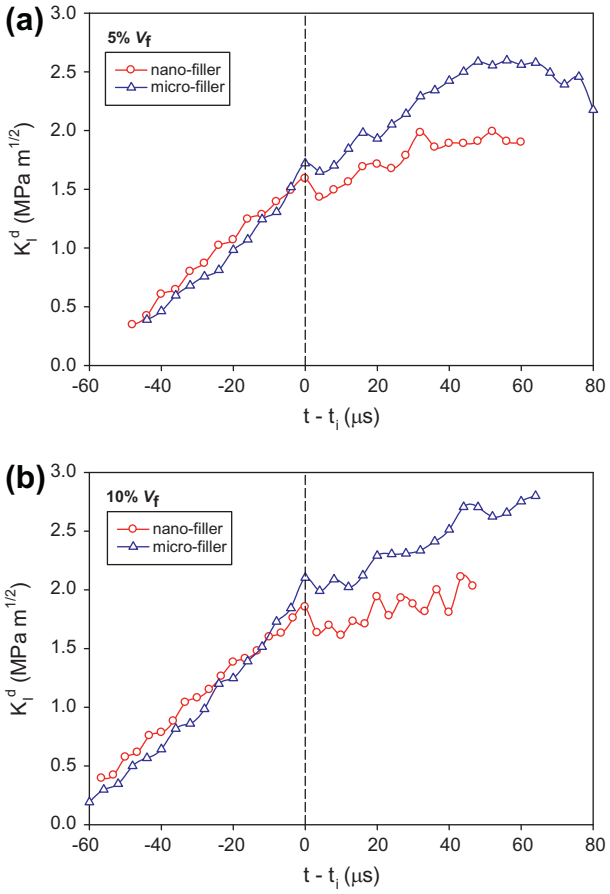

Fig. 15. Role of nano- vs. micro-fillers on mode-I dynamic SIF histories: (a) 5% V_f. (b) 10% V_f. (Time base is shifted such that $t - t_i = 0$ corresponds to crack-initiation as shown by the vertical dashed line.)

'mist' region. The micrograph for nano-filler with 5% V_f indicates a nonlinearly deformed (or torn) surface. Furthermore, the surface features resemble microscopic shear bands, seen as a narrow zone of intense slipping and tearing in the inset. The SEM micrograph for 10% nano-filler loading indicates the presence of parabolic markings in addition to all the features seen in the 5% filler case. These parabolic markings are possibly generated by sequential nucleation, growth and coalescence of microcracks (and/or slip bands) resulting in a rougher surface since microcracks or microcrack clusters form far ahead of the main crack and coalesce with it. A close-up view of the zone inside the parabolic marking can be seen in the inset showing microcracking and tearing. On the other hand, the SEM micrographs for 5% and 10% V_f micro-filler loadings show features such as tail lines and particle–matrix debonding. The fracture surface features from optical and SEM micrographs clearly indicate that nanocomposites showed extensive surface features compared to the corresponding micron-filler counterparts. Furthermore, nonlinear deformation and formation of microcracks around the crack-tip reduce the crack-tip stress concentration leading to shielding of the crack-tip. Therefore, the presence of a high concentration of macro and microcracks, slip bands, parabolic markings and high surface roughness suggest greater energy dissipation in the case of nano-filler modified epoxies, consistent with higher fracture toughness when compared to the ones with micro-filler *under quasi-static loading* conditions.

Fig. 18a and b show SEM micrographs of dynamically fractured surfaces (x–z plane) of nano- and micro-filler epoxies at 10% volume fraction, respectively. The arrow in these micrographs indicates crack propagation direction. The differences between the surface roughness features are rather striking. The surface roughness and ruggedness in Fig. 18a for nano-particle filled epoxy is lower than the micro-filler one. Some features such as crack front bowing and pinning can be seen but are less prominent than the micro-filler modified epoxy. A higher magnification view of the fracture surface morphology can be seen in the inset. The micrograph in Fig. 18b reveals particle–matrix debonding (see close-up view in the inset) and particle pullout which results in crack front trapping. It can also be noticed that the crack bows between micron-size particles indicating crack pinning. As micro-cracks leave the pinned positions, tail lines as well as step patterns in the direction of crack propagation appear.

Fig. 19 shows fractured surface profiles for nano- and micro-filler cases (10% V_f) and neat epoxy with an inset depicting crack growth and scanned region (x–z plane). In Fig. 19, x- represents

Table 3
Loading-rate effects on crack-initiation toughness of nano- and micro-filler reinforced epoxies.

V_f (%)	Quasi-static crack-initiation toughness K_{Ic} (MPa m$^{1/2}$)		Dynamic crack-initiation toughness K_{Ii}^d (MPa m1/2)	
	Nano-filler	Micro-filler	Nano-filler	Micro-filler
0	1.92	1.92	1.38	1.38
3	2.99	2.43	1.45	1.54
5	3.67	2.59	1.59	1.72
7	3.92	2.63	1.74	1.89
10	5.22	2.95	1.85	2.13

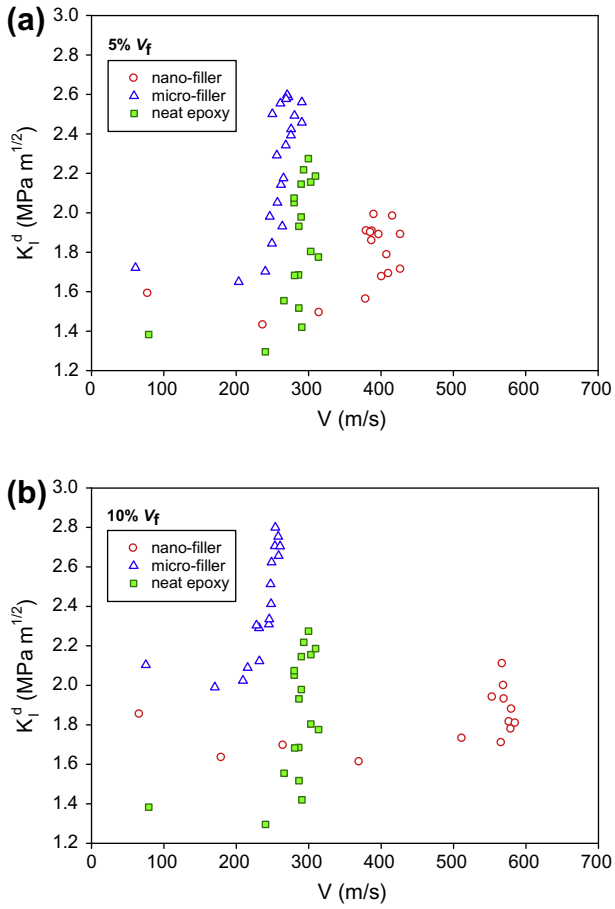

Fig. 16. K_I^d–V relationships for particle filled epoxies: (a) 5% V_f nano- and micro-filler. (b) 10% V_f nanoand micro-filler.

scanning length and y- denotes the asperity height. A scanning length of x = 15 mm was chosen in the stable crack growth region. The data was recorded at 3–4 different scan lines at different z-locations on either side of the centerline within the regions of interest. The scanned data obtained from the surface profiler was processed to get average roughness, R_a, using,

$$R_a = \frac{1}{N}\sum_{1}^{N}|y(x)| = \frac{1}{L}\int_0^L y\,dx \tag{8}$$

where N is the total number of data points collected, L is the scan length.

The surface profile of micro-filler case shows longer wavelengths and larger amplitudes relative to the nano-filler counterpart. The nano-particle filled epoxy and neat epoxy, on the other hand, show the least surface amplitude. The fracture-induced surface roughness (after discounting the roughness due to filler particle foot prints or bumps; see Kitey and Tippur [51]) was evaluated and found to be approximately 0.78 μm, 12.93 μm, 0.74 μm for nano-filler, micro-filler, and neat epoxy, respectively. Hence, it should be noted that for the same volume percentage of fillers embedded in epoxy, the fracture-induced roughness is higher in case of micro-filler under dynamic conditions. Thus, the qualitative as well as quantitative measurements show higher surface roughness for micro-particle filled epoxy than the nano-filler case suggesting higher energy dissipation and improved dynamic fracture performance in the former relative to the latter.

4.5. Discussion

The striking differences in quasi-static and dynamic fracture behaviors and parameters of nano- and micro-size silica filled epoxies are evident from the results presented above. As the macro scale fracture behaviors are related to events in the process zone [46] in the crack-tip vicinity, plausible explanations for these differences can be offered.

Under quasi-static loading conditions, a relatively smaller crack-tip process zone exists since all material points experience the applied load simultaneously. In case of nano-particle filled epoxy, the net interfacial surface area between the filler particle

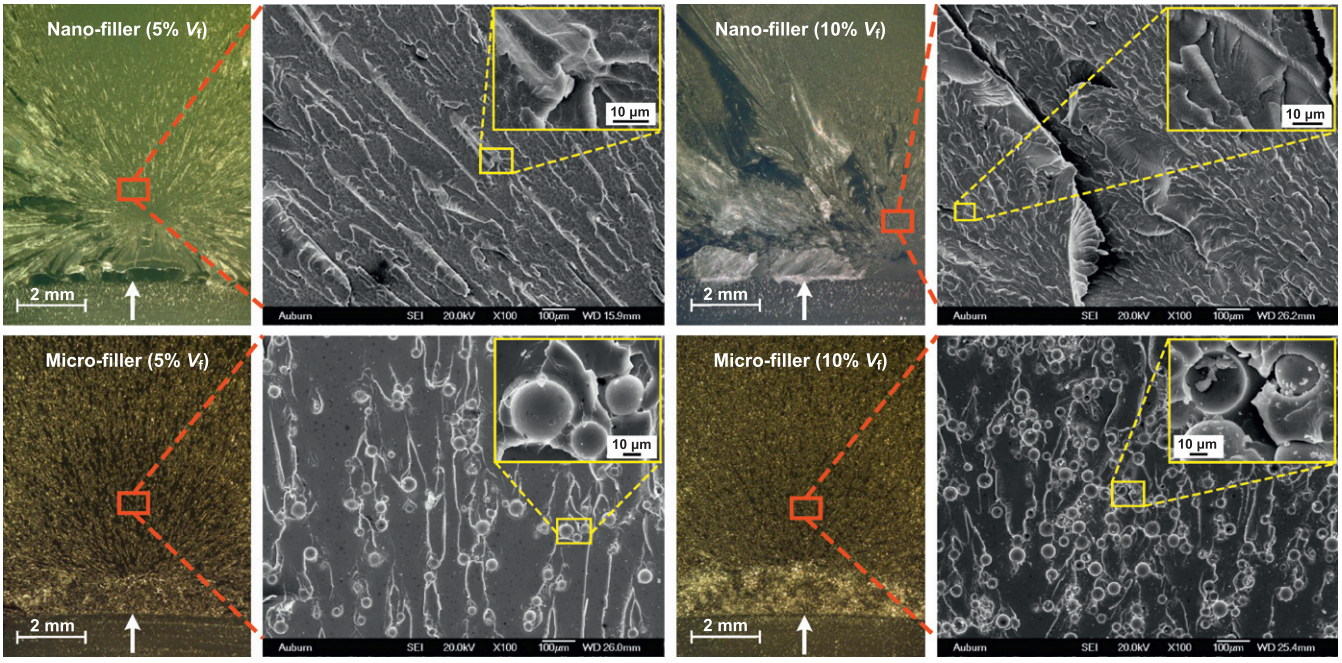

Fig. 17. Optical and SEM micrographs of quasi-static fracture surfaces of nano- and micro-filler modified epoxies at 5% and 10% volume fractions (V_f). The arrow in optical images indicates the initial crack-front as well as the direction of crack growth. The 'mirror', 'mist' and 'hackle' zones are clearly visible in optical images of nanocomposites.

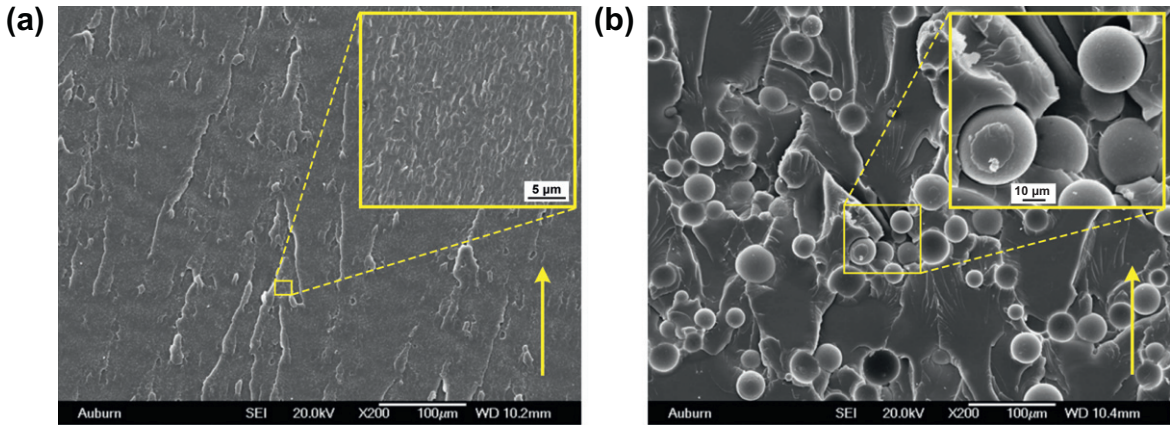

Fig. 18. SEM micrographs of dynamically fractured surfaces (x–z plane): (a) Nano-particle filled epoxy (10% V_f). (b) Micro-particle filled epoxy (10% V_f). The arrows indicate the direction of crack propagation.

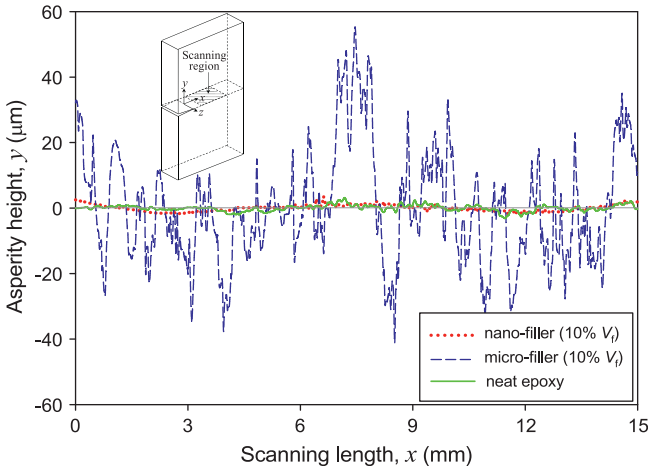

Fig. 19. Fracture surface profiles of dynamically fractured nano-particle filled epoxy (10% V_f), micro-particle filled epoxy (10% V_f) and neat epoxy specimens (inset shows schematic representation of crack growth and scanning region chosen for roughness measurements (x–z plane)).

and the matrix is $\sim 3.3 \times 10^5$ times that of the micron-size particles at the same volume fraction. Hence, for similar bond strength between the matrix and the filler, average interfacial stress is substantially lower in case of nanocomposites. The matrix reinforcement offered by the nano-particles, further mitigate crack initiation. On the other hand, the micro-fillers, due to the higher effective interfacial stress (due to lower interfacial area), would locally debond resulting in micro defects ahead of the crack-tip causing fracture at a lower far-field stress. Also, the average inter-particle spacing [52] $l = 2D(1 - V_f)/3V_f$, for a given volume fraction V_f with mean particle diameter D, is three orders of magnitude lower for the nano-filler case compared to the micro-filler counterparts. This results in lower interstitial gap reducing stress concentration effects in nano-particle filled epoxy when compared to the micron-size fillers, resulting in improved crack initiation toughness under quasi-static loading conditions.

Under dynamic loading conditions, however, the lower interfacial surface area and higher stress concentration effects present in micro-filler case produces filler-matrix interfacial debonding as stress waves propagate. Moreover, a propagating crack front is attracted and trapped by the weakened particle–matrix interfaces resulting in momentary deceleration and arrest [32]. This requires additional energy for reinitiation and further growth, producing higher apparent dynamic fracture toughness. In the nano-particle case, on the other hand, the lower matrix-filler interfacial stresses promote crack from deflecting away from interfaces producing sustained matrix crack growth (with the exception of crack pinning sites) at a relatively lower energy expenditure.

5. Conclusions

The role of nano- and micro-fillers (particle size-scale) on quasi-static and dynamic fracture behavior of particulate epoxy composites has been studied. The full-field method of 2D digital image correlation coupled with high-speed digital photography was used to evaluate dynamic fracture parameter histories. The results were supplemented by conducting fractographic examination and surface roughness measurements. The following are some of the major observations of this study:

- The particle size-scale did not produce discernible influence on elastic and physical properties at a given volume fraction in both nano- and micro-filler composites for all volume percentages (3–10%) studied.
- Both nano- and micro-fillers improved fracture toughness of epoxy under quasi-static loading. The quasi-static fracture toughness of nanocomposites was significantly higher than the micro-particle filled epoxies for any given volume fraction. Nanocomposite specimens containing 10% volume fraction filler yielded the greatest enhancement of fracture toughness (by about 78%) compared to the micro-filler counterparts at the same volume percentage.
- Dynamic fracture tests showed that with respect to neat epoxy the crack-tip velocities showed increasing and decreasing trends in nano- and micro-filler composites, respectively, with particle volume fractions. The average crack-tip velocities in nanocomposites were approximately 35%, 60%, 90%, 160% higher than that observed in the micro-filled specimens for the 3%, 5%, 7%, 10% volume fractions, respectively.
- Dynamic fracture toughness improved consistently with filler volume fraction for both nano- as well as micro-fillers when compared to neat epoxy. However, contrary to quasi-static fracture tests, the nanocomposites showed relatively lower dynamic crack-initiation toughness than the micro-particle filled ones with the same volume fraction of fillers.
- The K_I^d–V characteristics for both types of fillers were obtained. Nano-filler composites resulted in lower K_I^d over a wider range of velocities compared to the micro-filler counterparts. The ter-

minal velocities seen in the case of nano-filler specimens were significantly higher than the micro-filler ones under similar impact loading conditions.

- Fracture surfaces of quasi-statically failed nanocomposites showed very rough, highly textured surfaces containing mirror, mist and hackle zones, and these features markedly amplified with filler volume fraction. On the other hand, such features were muted in the case of micro-filler cases.
- Micrographs of dynamically fractured surfaces of micro-particle filled epoxy revealed higher surface roughness and ruggedness than the nanocomposites with features consistent with micro-cracks, crack front bowing, tails lines and crack pinning indicating improved crack growth resistance for micro-filler epoxies relative to nano-filler counterparts.
- Quantitative surface measurements showed that the fracture induced surface roughness was significantly higher in micro-filler composites than the nano-filler counterparts producing enhanced dynamic fracture toughness in the former case than in the latter case.

Acknowledgements

The authors would like to thank the National Science Foundation for supporting this research through a grant NSF-CMMI-0653816. Financial support from US Army Research Office for the high-speed digital camera purchase through a Grant DAAD19-02-10126 (DURIP) is also gratefully acknowledged.

References

[1] Lavengood RE, Nicolais L, Narkis M. A deformational mechanism in particulate-filled glassy polymers. J Appl Polym Sci 1973;17(4):1173–85.
[2] Mallick PK, Broutman LJ. Mechanical and fracture behaviour of glass bead filled epoxy composites. Mater Sci Eng 1975;18(1):63–73.
[3] Moloney AC, Kausch HH, Stieger HR. The fracture of particulate-filled epoxide resins. J Mater Sci 1983;18(1):208–16.
[4] Moloney A, Kausch H, Kaiser T, Beer H. Parameters determining the strength and toughness of particulate filled epoxide resins. J Mater Sci 1987;22(2):381–93.
[5] Spanoudakis J, Young RJ. Crack propagation in a glass particle-filled epoxy resin. J Mater Sci 1984;19(2):473–86.
[6] Roulin-Moloney AC, Cantwell WJ, Kausch HH. Parameters determining the strength and toughness of particulate-filled epoxy resins. Polym Compos 1987;8(5):314–23.
[7] Nakamura Y, Yamaguchi M, Okubo M, Matsumoto T. Effects of particle size on mechanical and impact properties of epoxy resin filled with spherical silica. J Appl Polym Sci 1992;45(7):1281–9.
[8] Nakamura Y, Okabe S, Iida T. Effects of particle shape, size and interfacial adhesion on the fracture strength of silica-filled epoxy resin. Polym Polym Compos 1999;7(3):177–86.
[9] Spanoudakis J, Young RJ. Crack propagation in a glass particle-filled epoxy resin. J Mater Sci 1984;19(2):487–96.
[10] Hsieh TH, Kinloch AJ, Masania K, Taylor AC, Sprenger S. The mechanisms and mechanics of the toughening of epoxy polymers modified with silica nanoparticles. Polymer 2010;51(26):6284–94.
[11] Reynaud E, Jouen T, Gauthier C, Vigier G, Varlet J. Nanofillers in polymeric matrix: a study on silica reinforced PA6. Polymer 2001;42(21):8759–68.
[12] Boesl BP, Bourne GR, Sankar BV. Insitu multiscale analysis of fracture mechanisms in nanocomposites. Compos Part B: Eng 2011;42(5):1157–63.
[13] Liu H-Y, Wang G-T, Mai Y-W, Zeng Y. On fracture toughness of nano-particle modified epoxy. Compos Part B: Eng 2011;42(8):2170–5.
[14] Rosso P, Ye L, Friedrich K, Sprenger S. A toughened epoxy resin by silica nanoparticle reinforcement. J Appl Polym Sci 2006;100(3):1849–55.
[15] Wetzel B, Rosso P, Haupert F, Friedrich K. Epoxy nanocomposites – fracture and toughening mechanisms. Eng Fract Mech 2006;73(16):2375–98.
[16] Liang YL, Pearson RA. Toughening mechanisms in epoxy-silica nanocomposites (ESNs). Polymer 2009;50(20):4895–905.
[17] Tsai JL, Hsiao H, Cheng YL. Investigating mechanical behaviors of silica nanoparticle reinforced composites. J Compos Mater 2010;44(4):505–24.
[18] Kwon S-C, Adachi T, Araki W. Temperature dependence of fracture toughness of silica/epoxy composites: related to microstructure of nano- and micro-particles packing. Compos Part B: Eng 2008;39(5):773–81.
[19] Johnsen BB, Kinloch AJ, Mohammed RD, Taylor AC, Sprenger S. Toughening mechanisms of nanoparticle-modified epoxy polymers. Polymer 2007;48(2):530–41.
[20] Jordan J, Jacob KI, Tannenbaum R, Sharaf MA, Jasiuk I. Experimental trends in polymer nanocomposites – a review. Mater Sci Eng A 2005;393(1–2):1–11.
[21] Sun L, Gibson RF, Gordaninejad F, Suhr J. Energy absorption capability of nanocomposites: a review. Compos Sci Technol 2009;69(14):2392–409.
[22] Fu S-Y, Feng X-Q, Lauke B, Mai Y-W. Effects of particle size, particle/matrix interface adhesion and particle loading on mechanical properties of particulate–polymer composites. Compos Part B: Eng 2008;39(6):933–61.
[23] Singh RP, Zhang M, Chan D. Toughening of a brittle thermosetting polymer: effects of reinforcement particle size and volume fraction. J Mater Sci 2002;37(4):781–8.
[24] Adachi T, Osaki M, Araki W, Kwon S-C. Fracture toughness of nano- and micro-spherical silica-particle-filled epoxy composites. Acta Mater 2008;56(9):2101–9.
[25] Hussain M, Nakahira A, Nishijima S, Niihara K. Fracture behavior and fracture toughness of particulate filled epoxy composites. Mater Lett 1996;27(1–2):21–5.
[26] Ng CB, Ash BJ, Schadler LS, Siegel RW. A study of the mechanical and permeability properties of nano- and micron-TiO_2 filled epoxy composites. Adv Compos Lett 2001;10(3):101–11.
[27] Ng CB, Schadler LS, Siegel RW. Synthesis and mechanical properties of TiO_2–epoxy nanocomposites. Nanostruct Mater 1999;12(1–4):507–10.
[28] Kitey R, Tippur HV. Role of particle size and filler-matrix adhesion on dynamic fracture of glass-filled epoxy. I. Macromeasurements. Acta Mater 2005;53(4):1153–65.
[29] Shukla A, Parameswaran V, Du Y, Evora V. Dynamic crack initiation and propagation in nanocomposite materials. Rev Adv Mater Sci 2006;13(1):47–58.
[30] Evora VMF, Shukla A. Fabrication, characterization, and dynamic behavior of polyester/TiO_2 nanocomposites. Mater Sci Eng A 2003;361(1–2):358–66.
[31] Evora VMF, Jain N, Shukla A. Stress intensity factor and crack velocity relationship for polyester/TiO2 nanocomposites. Exp Mech 2005;45(2):153–9.
[32] Jajam KC, Tippur HV. An experimental investigation of dynamic crack growth past a stiff inclusion. Eng Fract Mech 2011;78(6):1289–305.
[33] ASTM, D5045-96. Standard test methods for plane-strain fracture toughness and strain energy release rate of plastic materials. Annual Book of ASTM Standard1996. p. 325–33.
[34] Sanford RJ. Principles of Fracture Mechanics. Upper Saddle River, NJ, USA: Prentice Hall; 2003.
[35] Kirugulige MS, Tippur HV, Denney TS. Measurement of transient deformations using digital image correlation method and high-speed photography: application to dynamic fracture. Appl Opt 2007;46(22):5083–96.
[36] Kirugulige MS, Tippur HV. Measurement of fracture parameters for a mixed-mode crack driven by stress waves using image correlation technique and high-speed digital photography. Strain 2009;45(2):108–22.
[37] Lee D, Tippur H, Kirugulige M, Bogert P. Experimental study of dynamic crack growth in unidirectional graphite/epoxy composites using digital image correlation method and high-speed photography. J Compos Mater 2009;43(19):2081–108.
[38] Prautzsch H, Boehm W, Paluszny M. Bézier and B-spline techniques. Berlin Heidelberg New York: Springer-Verlag; 2002.
[39] Nishioka T, Atluri SN. Path-independent integrals, energy release rates, and general solutions of near-tip fields in mixed-mode dynamic fracture mechanics. Eng Fract Mech 1983;18(1):1–22.
[40] Tippur HV, Krishnaswamy S, Rosakis AJ. Optical mapping of crack tip deformations using the mehods of transmission and reflection coherent gradient sensing: a study of crack tip <ceitalic>K</ceitalic> -dominance. Int J Fract 1991;52(2):91–117.
[41] Irwin G, Dally J, Kobayashi T, Fourney W, Etheridge M, Rossmanith H. On the determination of the <ceitalic>å-K</ceitalic> relationship for birefringent polymers. Exp Mech 1979;19(4):121–8.
[42] Kobayashi T, Dally JW. Dynamic photoelastic determination of the *å–K* relation for 4340 alloy steel. Crack Arrest Methodology and Applications, ASTM STP 711, GT Hann and MF Kanninen, editors, American Society for Testing Materials. 1980:189-210.
[43] Dally JW, Fourney WL, Irwin GR. On the uniqueness of the stress intensity factor — crack velocity relationship. Int J Fract 1985;27(3):159–68.
[44] Knauss WG, Ravi-Chandar K. Some basic problems in stress wave dominated fracture. Int J Fract 1985;27(3):127–43.
[45] Shukla A, Nigam H. A note on the stress intensity factor and crack velocity relationship for homalite 100. Eng Fract Mech 1986;25(1):91–102.
[46] Broberg KB. Crack and fracture. Cambridge: Academic Press; 1999.
[47] Arakawa K, Takahashi K. Relationships between fracture parameters and fracture surface roughness of brittle polymers. Int J Fract 1991;48(2):103–14.
[48] Takahashi K, Kido M, Arakawa K. Fracture roughness evolution during mode i dynamic crack propagation in brittle materials. Int J Fract 1998;90(1):119–31.
[49] Sharon E, Gross SP, Fineberg J. Energy dissipation in dynamic fracture. Phys Rev Lett 1996;76(12):2117.
[50] Lampman S. Characterization and failure analysis of plastics. USA: ASM International, Materials Park, OH; 2003.
[51] Kitey R, Tippur HV. Role of particle size and filler-matrix adhesion on dynamic fracture of glass-filled epoxy. II. Linkage between macro- and micro-measurements. Acta Mater 2005;53(4):1167–78.
[52] Fullman RL. Measurement of particle sizes in opaque bodies. Trans Am Inst Mining Metall Eng 1953;197(3):447–52.